Eur. Phys. J. A **14**, 309–316 (2002)
DOI 10.1140/epja/i2002-10012-2

THE EUROPEAN PHYSICAL JOURNAL A

Count fluctuation analysis in the triaxial strongly deformed potential well of ^{163}Lu

S.W. Ødegård[1,2,a], B. Herskind[2], T. Døssing[2], G.B. Hagemann[2], D.R. Jensen[2], G. Sletten[2], J.N. Wilson[2], S. Leoni[3], P.O. Tjøm[1], P. Bednarczyk[4], and D. Curien[4]

[1] Department of Physics, University of Oslo, PB 1048 Blindern, N-0316 Oslo, Norway
[2] The Niels Bohr Institute, Blegdamsvej 17, DK-2100 Copenhagen Ø, Denmark
[3] Dipartimento di Fisica and INFN, Sezione di Milano, Milano, Italy
[4] IReS, 23 rue du Loess, BP28 F-67037, Strasbourg, France

Received: 4 January 2002 / Revised version: 22 April 2002
Communicated by C. Signorini

Abstract. High-spin properties of the triaxial strongly deformed potential well in ^{163}Lu at excitation energies above resolvable bands have been investigated. Gated E_γ-E_γ spectra display clear ridges with moments of inertia corresponding to those observed for the discrete strongly deformed bands. A fluctuation analysis of the ridges yields a number of two-step paths of ≈ 40 and ≈ 20, when gating on triaxial strongly or normally deformed bands, respectively. These results show that a potential well at large deformation coexists with the normally deformed well, and indicate a mixing between states in the two wells at higher excitation energy.

PACS. 21.10.-k Properties of nuclei; nuclear energy levels – 21.10.Re Collective levels – 24.60.Ky Fluctuation phenomena – 27.70.+q $150 \leq A \leq 189$

1 Introduction

Rotational bands with large deformation have been observed in several nuclei in the $Z \sim 71$, $N \sim 92$ region. In the odd proton isotopes ^{163,164,165,167}Lu [1–5], those bands are interpreted as based on the deformation-driving proton $i_{13/2}$ intruder configuration, while in the even-even ^{168}Hf [6] nucleus, the observed weakly populated bands are less well understood. The transition quadrupole moments determined in several lifetime measurements on ^{163,164}Lu [2,7] and ^{168}Hf [6] indicate a substantially larger deformation than that of the normally deformed bands in these nuclei, in accordance with the values of the dynamic moments of inertia.

Cranking calculations based on the modified oscillator potential with the code "Ultimate Cranker" (UC) [8,9] predict local minima in the potential-energy surface at triaxial deformations with $\epsilon_2 \sim 0.4$ and with a triaxiality of $\gamma \sim \pm 20°$ [4]. In the calculations, local minima at this deformation are found for all combinations of parity and signature, and originate from the opening of a shell gap at 94 neutrons for this triaxial deformation.

The recent observation of a one-phonon wobbling excitation [10], and possibly a two-phonon excitation [11], is the first firm experimental evidence of the triaxiality of these states, in ^{163}Lu.

Under certain conditions one may expect a multitude of wobbling excitations based on each of the triaxial configurations [12], which opens up the possibility for a very large number of bands. In this way, the breaking of the axial symmetry may lead to a higher level density in the triaxial-deformed potential well as compared to the axial-symmetric normal-deformed well [12]. To investigate the properties of the nucleus at excitation energies above the energy of the resolved discrete bands, tools that go beyond the discrete line spectroscopy analysis are needed. One such tool is the fluctuation analysis of counts in the E_γ-E_γ energy spectrum [13].

2 The region of unresolved bands

Normally deformed nuclei with collective rotation typically display around 30–50 discrete rotational paths. This number is limited due to the onset of fragmentation of the rotational transition strength, which takes place around an excitation energy above yrast of about $U_0 \approx 800$ keV. U_0 is defined as the energy where the rotational strength out of each state of angular momentum I on the average fragments into two transitions to states of $I - 2$. However, large deviations from this average behavior are

[a] e-mail: s.w.odegard@fys.uio.no

expected and also predicted in calculations of rotational bands, mixed by a residual interaction [14]. Some rotational bands may avoid fragmentation at energies well above U_0, keeping the rotational energy correlation along the band. The fragmentation of rotational strength is also accompanied by a loss of rotational energy correlations, referred to as damping of the rotational motion [15].

In the E_γ-E_γ spectra, consecutive transitions belonging to unresolved discrete bands at excitation energies below the damping region will form ridges [13] characterized by the relation $(E_{\gamma 1} - E_{\gamma 2} \approx 4\hbar^2/\mathcal{J}^{(2)})$, where $\mathcal{J}^{(2)}$ is the dynamic moment of inertia. The ridges are formed by the unresolved *regular bands* existing at low excitation energy where the level density is low. These bands are too weak to be identified in the discrete line analysis, and they may also fragment at higher or lower angular momentum, *e.g.*, energy correlations are only kept for a few steps [16].

The central valley at $E_{\gamma 1} \approx E_{\gamma 2}$ contains coincidences for which the fragmentation has completely destroyed the rotational energy correlations. They originate from levels higher in excitation energy ($> U_0$), where the rotational transition strength will be fragmented over many states.

2.1 The fluctuation analysis and number of two-step paths

The analysis of count fluctuations in the E_γ-E_γ spectra is based on the fact that there is a limit to the number of possible decay paths available to the γ-cascades. If the number of observed events is greater than the number of available paths, the fluctuations of the spectrum will be stronger than purely statistical fluctuations. These fluctuations, expressed by the moments μ_1 and μ_2, are determined by the number of available paths. The relative magnitude of such fluctuations visible in a spectrum and expressed by the ratio $\sqrt{\mu_2}/\mu_1$, will not decrease with increased counting statistics unlike randomly distributed statistical fluctuations.

The goal of the statistical analysis of the count fluctuations in the E_γ-E_γ spectrum is to determine the number of paths available to the nucleus in the γ-decay at particular excitation energy and spin regions. For the analysis of the two-dimensional coincidence matrices, the number of two-step paths, $N^{(2)}_{\rm path}$, can be expressed by [13]

$$N^{(2)}_{\rm path} = \frac{N_{\rm eve}}{\left(\frac{\mu_2}{\mu_1} - 1\right)} \frac{P^{(2)}}{P^{(1)}}. \qquad (1)$$

The moments, μ_1 and μ_2 of the fluctuations, and the number of events, $N_{\rm eve}$, are found by integrating over a $4\hbar^2/\mathcal{J}^{(2)} \times 4\hbar^2/\mathcal{J}^{(2)}$ region of the matrices. For rotational decay, the average distance between two consecutive transitions, $4\hbar^2/\mathcal{J}^{(2)}$, is the natural energy scale, and all cascades originating at a high angular momentum will on the average place one coincidence within each $4\hbar^2/\mathcal{J}^{(2)} \times 4\hbar^2/\mathcal{J}^{(2)}$ interval. The factor $P^{(2)}/P^{(1)}$ corrects for the dilution of the fluctuations due to the finite energy resolution of the detectors.

The basic limitation of the fluctuation analysis is illustrated in eq. (1) by the term $(\frac{\mu_2}{\mu_1} - 1)$. The number one in the denominator is due to the statistical counting fluctuations superimposed on the fluctuations caused by the limited number of paths. Thus, in the limit of μ_2/μ_1 approaching one, the analysis only provides a lower limit to the number of paths.

3 Experimental methods and analysis

The 152 MeV beam used in the reaction ^{139}La(^{29}Si, 5n)^{163}Lu, with a thin self-supporting target, was delivered by the Vivitron tandem accelerator in Strasbourg. The Euroball IV set-up [17], at that time comprising 15 cluster detectors, 25 clover detectors, 26 tapered detectors, and the inner ball was used in the detection of the reaction products. With the triggering conditions of 3 or more suppressed γ-rays in the Ge detectors and 8 or more γ-rays detected in the BGO inner ball, approximately 2.4×10^9 events were collected. Further experimental details can be found in refs. [10,11].

Three different E_γ-E_γ coincidence matrices were sorted from the dataset: One matrix, with no gating condition, containing the total γ-intensity of E_γ-E_γ coincidences of the reaction (NG-matrix), and two matrices gated on transitions in the normal-deformed (ND-matrix) and triaxial strongly deformed (TSD-matrix) parts of the level scheme, respectively.

The NG-matrix contains coincidences mainly from the strong reaction channels populating ^{163}Lu and ^{164}Lu, in addition to a smaller number of coincidences from the other populated channels. Useful gates are only those which are not contaminated and carry a large intensity. The ND gates were selected to have no contamination from transitions in any of the discrete TSD transitions as well as from ND transitions through which the TSD bands decay. The TSD gates were selected among the low-spin members of the yrast TSD band, which have no overlap with any ND transition. These restrictive criteria strongly limit the number of possible gates to the five ND and five TSD gates shown in fig. 1, which cover comparable spin regions, and also produce matrices of intensities differing by less than 10%. The ND-matrix is gated on transitions in both positive- and negative-parity bands and contains coincidences from all combinations of parity and signature. In fig. 2 spectra gated on one transition energy in the TSD yrast band are shown for both the TSD-gated matrix and the ND-gated matrix, to illustrate that no sign of the strongly populated TSD band can be found in the ND-gated matrix. The TSD-matrix is gated at low spin on transitions in the yrast band in the strongly deformed triaxial potential well. The two gated matrices were corrected for the background under the peaks used in the gate. Ideally this would be done by setting background gates next to the peaks and then normalizing to the width of the gates. But as there are more than 1200 identified transitions in the energy region between 100 and 1300 keV in the dataset, finding regions

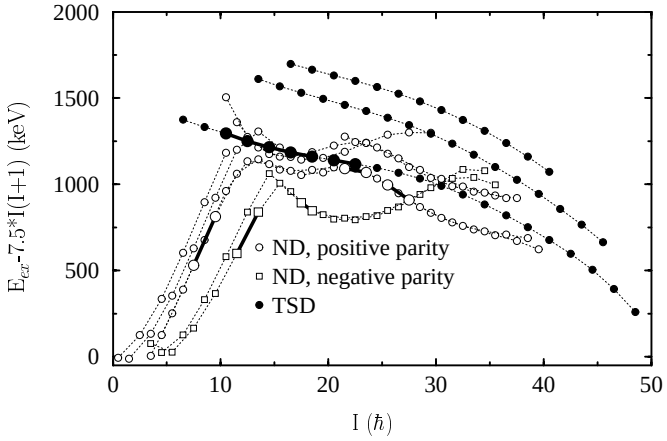

Fig. 1. Excitation energy relative to a rigid rotor for selected normal-deformed and TSD bands in ^{163}Lu. The transitions used for creating the gated matrices are marked with a solid line together with a larger symbol for the initial and final states.

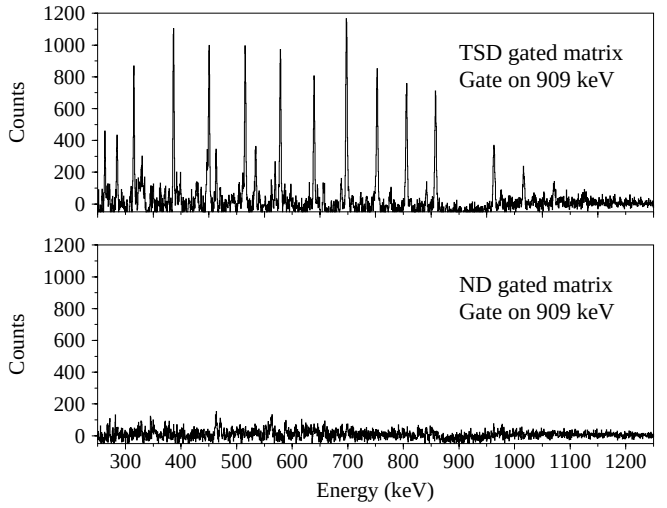

Fig. 2. Gates on the 909 keV transition of the yrast TSD band in the TSD-gated (top) and ND-gated (bottom) matrices before the subtraction of peaks.

free of transitions that would contaminate the background gate is impossible. The best attempt in this case is to use the full 2-dimensional projection properly normalized as the background spectrum. The matrices have been compressed from the experimental resolution of 0.5 keV/ch to 2 keV/ch before Compton scattering and other uncorrelated events were removed by a Cor background subtraction [18]. In this procedure, an uncorrelated 2-dimensional spectrum $\mathrm{Uncor}(x,y)$ is calculated from the original spectrum $\mathrm{Raw}(x,y)$ by

$$\mathrm{Uncor}(x,y) = \frac{\sum_x \mathrm{Raw}(x,y) \sum_y \mathrm{Raw}(x,y)}{\sum_{x,y} \mathrm{Raw}(x,y)}.$$

Since the uncorrelated spectrum $\mathrm{Uncor}(x,y)$ still contains the true photopeak coincidences it may be normalized by a factor $C < 1$, chosen as $C = 0.7$ in the present analysis, in accordance with previous experience [13], before subtraction from the $\mathrm{Raw}(x,y)$ spectrum. The influence from the choice of the number C was investigated and found negligible within a variation of $\pm 10\%$. The background-subtracted spectrum dominated by correlated events, $\mathrm{Cor}(x,y)$, can then be expressed as

$$\mathrm{Cor}(x,y) = \mathrm{Raw}(x,y) - C \cdot \mathrm{Uncor}(x,y).$$

Due to the fact that the strongly populated peaks from low-lying known band structures distort the fluctuation analysis, peaks originating from coincidences of identified transitions in the discrete line analysis were removed from all the matrices in the energy region of interest for the analysis. This was done by an extended version of the RADWARE package [19], and fig. 3 shows the gated matrices both before and after the peak subtraction. The resulting peak-subtracted $\mathrm{Cor}(x,y)$ matrices are the basis for the fluctuation analysis.

3.1 The statistical analysis program STATFIT

The fluctuations of counts in the resulting $\mathrm{Cor}(x,y)$ matrices can be expressed in terms of the first and second moments with respect to a smooth fit of the same matrix. The program STATFIT [13,20] was used to extract the moments μ_1 and μ_2 from the experimental data. A smooth fit to the spectrum, $\mathrm{Fit}(x,y)$, was calculated by performing a third-order polynomial fit in a window of size 9×9 channels, for each point (x_0, y_0) in the $\mathrm{Cor}(x,y)$ spectrum. A different procedure with a Gaussian smoothing function with a standard deviation of 3 channels was also tested, giving similar results as the polynomial fit. The moments $\mu_1(x_0,y_0)$ and $\mu_2(x_0,y_0)$ in the single channel (x_0,y_0) were calculated by selecting a window of size 9×9 channels around (x_0,y_0) and then point by point within the window evaluating the expressions $\mathrm{Cor}(x,y) f(x-x_0, y-y_0)$ and $(\mathrm{Cor}(x,y) - \mathrm{Fit}(x,y))^2 f(x-x_0, y-y_0)$. The function $f(x-x_0, y-y_0)$ is a properly normalized Gaussian weighting function with a standard deviation σ of one channel, corresponding to the experimental resolution, centered around (x_0,y_0). The moments are extracted according to

$$\mu_1(x_0,y_0) = \sum_{x,y} \mathrm{Cor}(x,y) f(x-x_0, y-y_0)$$

and

$$\mu_2(x_0,y_0) = \sum_{x,y} (\mathrm{Cor}(x,y) - \mathrm{Fit}(x,y))^2 f(x-x_0, y-y_0).$$

This procedure was repeated for each of the channels in the spectra.

Figure 4 shows the distribution of consecutive in-band coincidences from the discrete line analysis plotted in a similar way as fig. 3 but rotated by 45°. Comparing fig. 3 and fig. 4, one sees from the ridge gated by the TSD band

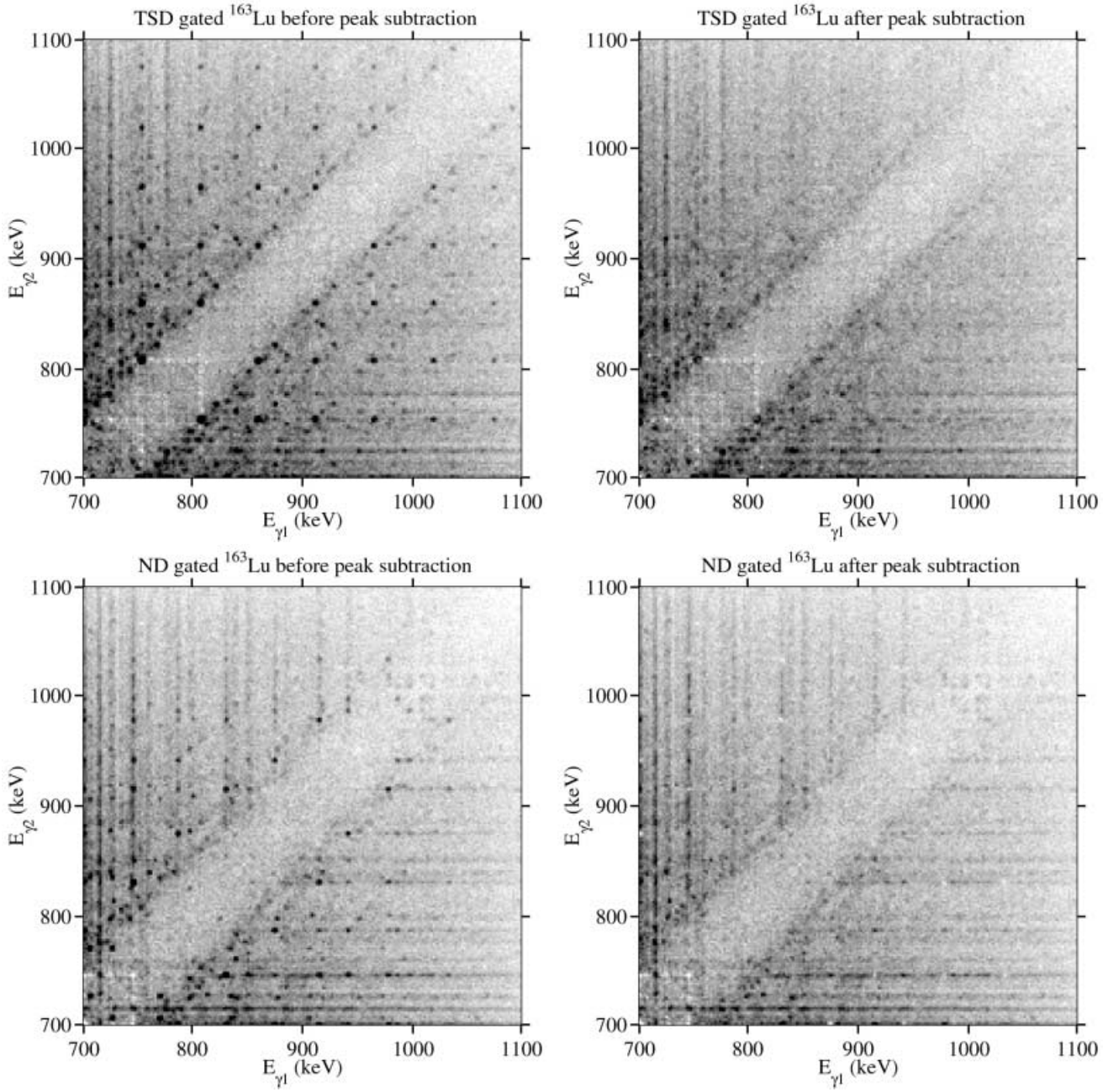

Fig. 3. Cor background-subtracted TSD- and ND-gated matrices before and after the subtraction of known peaks in the relevant energy region.

that the unresolved TSD ridge and the resolved bands behave in a similar way with respect to the moment of inertia, whereas for the ND gate the picture is less clear. If also the unresolved ND bands behave in accordance with the resolved ND bands, a separation of the two ridges originating from TSD and ND unresolved bands should be possible in the region from 750 keV to 1100 keV, which is basically free of crossings. Thus, cuts of a width of 58 keV perpendicular to the $E_{\gamma_1} = E_{\gamma_2}$ diagonal were made for $(E_{\gamma_1} + E_{\gamma_2})/2 = 790$ keV up to 1060 keV in steps of 30 keV in the 2-dimensional matrices of μ_1 and μ_2. Examples of cuts of the μ_1 and μ_2 matrices for the TSD-gated and ND-gated cases are shown in fig. 5 and fig. 6, respectively. For the ridge analysis, the experimental peak intensities of μ_1 and μ_2 are extracted by Gauss fitting the peaks in the cuts, around $(E_{\gamma_1} - E_{\gamma_2}) \approx 54$ keV, corresponding to the moment of inertia $4\hbar^2/\mathcal{J}^{(2)}$ of the first ridge. Cuts appearing to have unremoved peaks were omitted, cf. fig. 7.

4 Experimental results

4.1 Results on the ridges

All events building up the ridges are assumed to be true photopeak-photopeak coincidences. Thus, values of μ_1

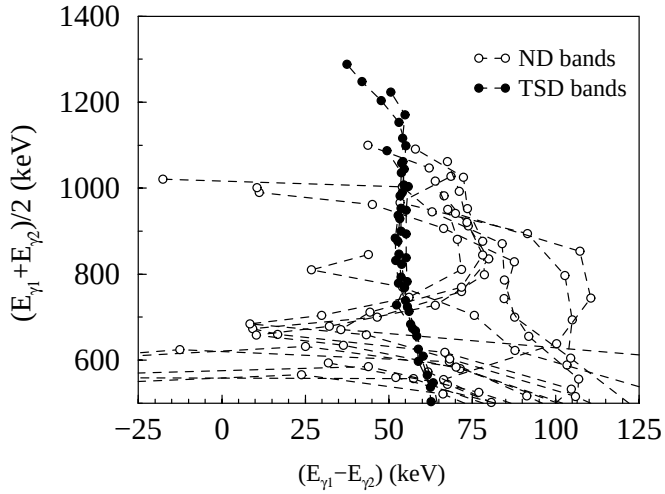

Fig. 4. Consecutive E_γ coincidences in the bands identified in the discrete line analysis of ^{163}Lu.

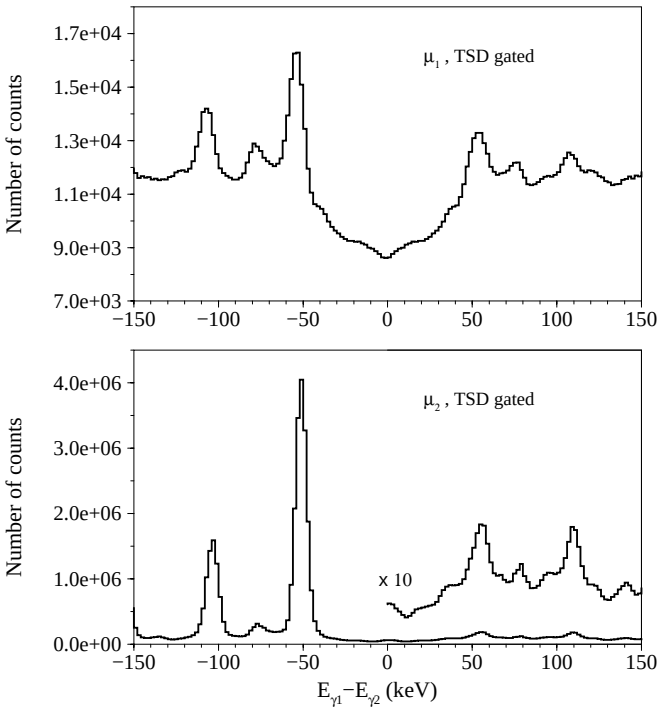

Fig. 5. Cuts in the TSD-gated μ_1 and μ_2 matrices at $(E_{\gamma_1} + E_{\gamma_2})/2 = 850$ keV. The left side, $(E_{\gamma_1} - E_{\gamma_2}) < 0$, shows the values of the moments without the peak subtraction while the right side shows the results after the peak subtraction procedure.

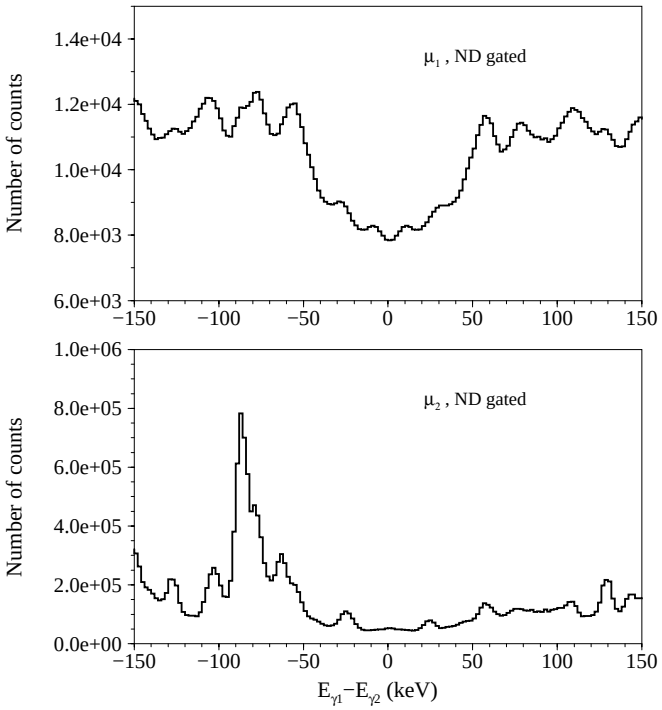

Fig. 6. Cuts in the ND-gated μ_1 and μ_2 matrices at $(E_{\gamma_1} + E_{\gamma_2})/2 = 820$ keV. The left side, $(E_{\gamma_1} - E_{\gamma_2}) < 0$, shows the values of the moments without the peak subtraction while the right side shows the results after the peak subtraction procedure.

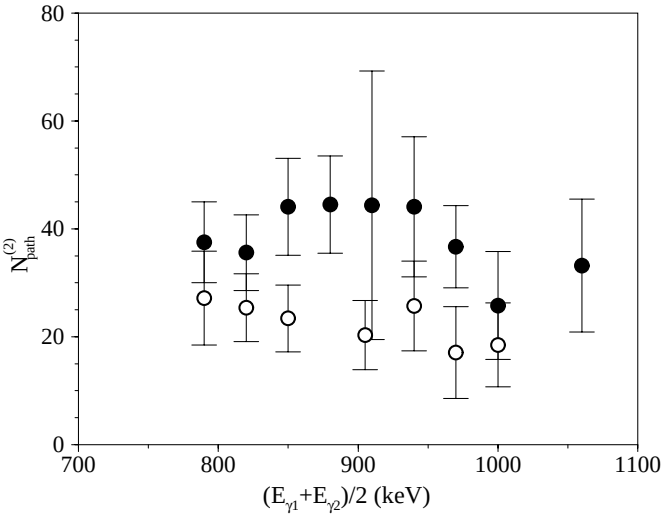

Fig. 7. Number of two-step paths along the TSD ridge in the TSD-gated matrix (filled circles) and ND-gated matrix (open circles). The background of the μ_2 spectra has been considered in the evaluation of the error bars.

and μ_2 can be extracted from the $\mathrm{Cor}(x, y)$ background-subtracted matrices, and the number of paths in the 58 keV wide cut of the matrix is given directly by eq. (1). The numbers were normalized with the assumption that the TSD bands in average deposit one event in a 54 keV wide cut. The resulting number of paths for the TSD ridge, from the TSD- and ND-gated matrices, are displayed in fig. 7. For the TSD-gated matrix, the average number of paths along the TSD ridge is 38.4 ± 6.5, while for the ND-gated matrix, the number of paths along the same ridge is 22.5 ± 3.9. The intensities of the yrast TSD band in the TSD-gated matrix and the TSD ridge in the two gated matrices are shown in fig. 8. The exponential behavior of the intensities display the general cooling of the nucleus

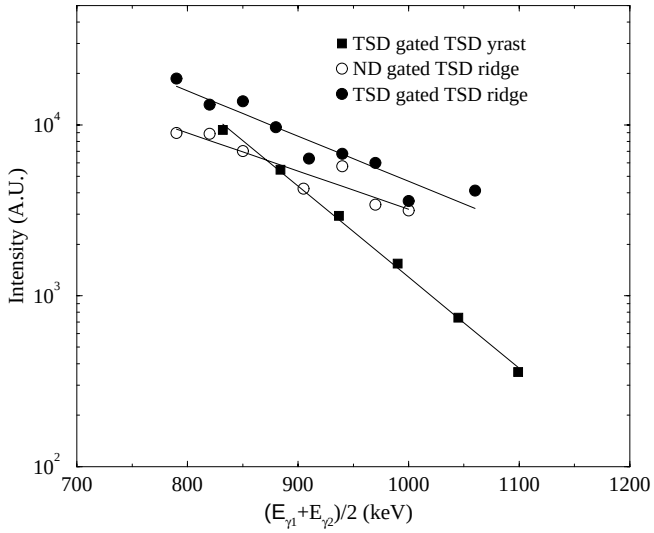

Fig. 8. The intensity of the yrast TSD band and TSD ridge in the TSD-gated matrix together with the TSD ridge in the ND-gated matrix. The intensity of the ridge from the ND-gated matrix has been normalized by the ratio of the total intensity in the gated matrices. The lines represent exponential fits of the data points.

in the decay cascades. With decreasing angular momentum, an increasing intensity goes to cold regular bands and eventually down into the lowest-lying resolved bands. The factor of about two of the intensity of the TSD-gated ridge relative to the ND-gated in fig. 8 is in accordance with the ratio between the numbers of paths in fig. 7.

4.2 Results in the valley

For the valley analysis the fraction, f, of photopeak-photopeak coincidences needs to be included in the evaluation of the number of paths, since coincidences including non-photopeak energies cannot be distinguished. The fraction f is deduced from the Raw(x, y) spectrum and a 2D unfolded spectrum. Statistically significant results could be obtained only for the total ungated spectrum in the present analysis. (For the gated spectra we always obtained $\mu_2 \approx \mu_1$ in the valley.) For the ungated spectrum, the first moment, μ_1 is extracted directly from the original Raw(x, y) spectrum before any background subtraction, while the second moment is evaluated for the Cor-subtracted spectrum. The number of two-step paths in the valley is given by

$$N^{(2)}_{\rm path} = \frac{N_{\rm eve}}{\left(\frac{\mu_2}{\mu_1} - 1\right)} \frac{P^{(2)}}{P^{(1)}} f^2.$$

The valley was analyzed using channels of 4 keV and perpendicular cuts of width 60 keV. The result, shown in fig. 9, indicates a number of two-step paths close to 10^6 at an average transition energy around 1100 keV, similar to the number of paths found for normally deformed nuclei [13]. The drop around $(E_{\gamma_1} + E_{\gamma_2})/2 \approx 1000$ keV

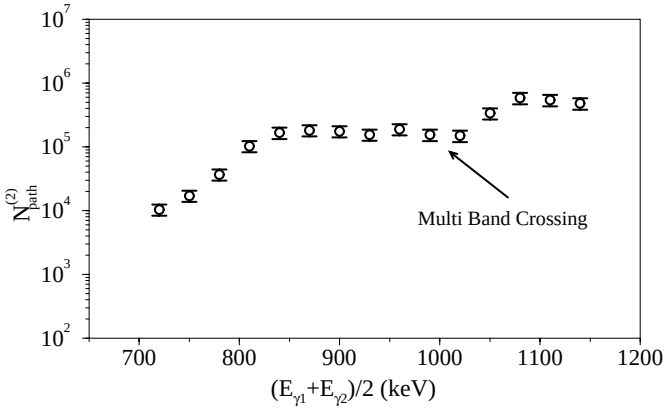

Fig. 9. Number of two-step paths along the valley in the ungated matrix.

is due to a multi-band crossing, which contaminates the valley in the region of $(E_{\gamma_1} + E_{\gamma_2})/2$ between 975 keV and 1025 keV.

5 Discussion

The average number of ≈ 40 two-step paths in the TSD ridge of the TSD-gated matrix is rather large and comparable to values for all four parity-signature combinations in axially symmetric nuclei. This large number indicates that there is a separate triaxial potential well at a substantially different deformation coexisting with the normal-deformed potential well. If the gating by the lowest TSD band selects among the excited bands according to parity and/or signature, in principle up to 4×40 regular TSD bands could exist in the TSD well.

The large number of paths could be a consequence of the breaking of the axial symmetry, which will lead to an increased number of high-spin states for any given I. However, this may increase the level density and thereby possibly lower the threshold of the onset of damping, U_0, which is closely related to the spacing between the levels. In that case, the number of discrete paths available in the decay would probably not be expected to increase, and no clear conclusions of the impact of a triaxial shape can be drawn. Also, the rather strong population of the yrast TSD compared to the excited TSD bands raise the question whether a comparison to previously investigated ND cases can be justified.

Another explanation for the large number of two-step paths may be related to the similarity of alignments and moments of inertia of the discrete TSD bands. This resembles the situation in the Hg-Pb region where theory predicts 150–200 discrete superdeformed bands below the onset of damping [21].

In the ND-gated matrix, ≈ 20 paths in the TSD ridge are observed. This is indeed surprising, since none of the lower-lying observed discrete TSD bands can be seen in the ND-gated matrix, cf. fig. 2. This indicates that about fifty percent of TSD paths feed the ND potential well, due to a mixing of the unresolved states in the two minima at excitation energies right below the onset of damping,

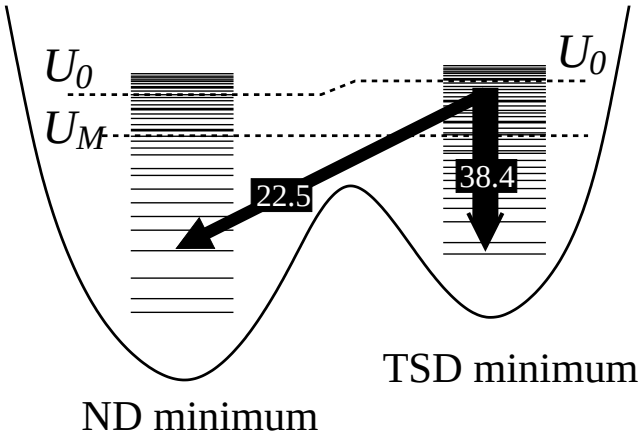

Fig. 10. Schematic illustration of the two potential wells. U_0 indicates the energy of the onset of damping, while $U_{\rm M}$ indicates the threshold of mixing between the states in the TSD and ND potential wells.

but above a certain energy $U_{\rm M}$, where mixing sets in and induces cross-talk between the potential wells. At lower excitation energy, the potential barrier is most probably too large, and the bands closer to the TSD yrast states stay in the TSD well. When they finally decay to ND states it happens at such a low angular momentum that the decay cascade bypasses the ND gates used. The two minima and their states are illustrated schematically in fig. 10. The two potential wells may be separated by a barrier at lower energy, but a small mixing between the TSD and ND states occur at excitation energies above $U_{\rm M}$. It should be noted that $U_{\rm M}$ like U_0 does not represent a sharply defined limiting excitation energy. Alternatively, the observed types of decay paths may not originate from the same states. This may be investigated by a covariance analysis [22], which however requires better statistics than allowed in the present experiment.

Due to the limitation of the statistics in the data set, only the non-gated matrix could be analyzed in the valley. Thus, no conclusions regarding the consequences of the coexistence of a triaxially deformed second potential well on the number of paths in the damped region could be drawn.

In conclusion, the analysis shows that there are ≈ 40 two-step paths with a moment of inertia similar to the low-lying TSD bands observed in ^{163}Lu. About half of these feed the ND structures in the nucleus, most probably due to mixing of states across the barrier separating the two shapes.

This research is supported by the EU TMR project No. ERBFMGECT980145, the EU TMR network project, contract No. ERBFMRXCT970123, the Danish Science Foundation and the Research Council of Norway.

References

1. W. Schmitz, C.X. Yang, H. Hübel, A.P. Byrne, R. Müsseler, N. Singh, K.H. Maier, A. Kuhnert, R. Wyss, Nucl. Phys. A **539**, 112 (1992).
2. W. Schmitz, H. Hübel, C.X. Yang, G. Baldsiefen, U. Birkental, G. Fröhlingsdorf, D. Mehta, R. Müsseler, M. Neffgen, P. Willsau, J. Gascon, G.B. Hagemann, A. Maj, D. Müller, J. Nyberg, M. Piiparinen, A. Virtanen, R. Wyss, Phys. Lett. B **303**, 230 (1993).
3. S. Törmänen, S.W. Ødegård, G.B. Hagemann, A. Harsmann, M. Bergström, R.A. Bark, B. Herskind, G. Sletten, P.O. Tjøm, A. Görgen, H. Hübel, B. Aengenvoort, U.J. van Severen, C. Fahlander, D. Napoli, S. Lenzi, C. Petrache, C. Ur, H.J. Jensen, H. Ryde, R. Bengtsson, A. Bracco, S. Frattini, R. Chapman, D.M. Cullen, S.L. King, Phys. Lett. B **454**, 8 (1999).
4. H. Schnack-Petersen, R. Bengtsson, R.A. Bark, P. Bosetti, A. Brockstedt, H. Carlsson, L.P. Ekström, G.B. Hagemann, B. Herskind, F. Ingebretsen, H.J. Jensen, S. Leoni, A. Nordlund, H. Ryde, P.O. Tjøm, C.X. Yang, Nucl. Phys. A **594**, 175 (1995).
5. C.X. Yang, X.G. Wu, H. Zheng, X.A. Liu, Y.S. Chen, C.W. Shen, Y.J. Ma, J.B. Lu, S. Wen, G.S. Li, S.G. Li, G.J. Yuan, P.K. Weng, Y.Z. Liu, Eur. Phys. J. A **1**, 237 (1998).
6. H. Amro, P.G. Varmette, W.C. Ma, B. Herskind, G.B. Hagemann, G. Sletten, R.V.F. Janssens, M. Bergström, A. Bracco, M. Carpenter, J. Domscheit, S. Frattini, D.J. Hartley, H. Hübel, T.L. Khoo, F. Kondev, T. Lauritsen, C.J. Lister, B. Million, S.W. Ødegård, R.B. Piercey, L.L. Riedinger, K.A. Schmidt, S. Siem, I. Wiedenhöver, J.A. Winger, Phys. Lett. B **506**, 39 (2001).
7. G. Schönwasser, H. Hübel, G.B. Hagemann, J. Domscheit, A. Görgen, B. Herskind, G. Sletten, J.N. Wilson, D.R. Napoli, C. Rossi-Alvarez, D. Bazzacco, R. Bengtsson, H. Ryde, P.O. Tjøm, S.W. Ødegård, Eur. Phys. J. A **13**, 291 (2002).
8. T. Bengtsson, Nucl. Phys. A **496** (1989) 56; **512**, 124 (1990).
9. R. Bengtsson, `www.matfys.lth.se/~ragnar/ultimate.html`.
10. S.W. Ødegård, G.B. Hagemann, D.R. Jensen, M.Bergström, B. Herskind, G. Sletten, S. Törmänen, J.N. Wilson, P.O. Tjøm, I. Hamamoto, K. Spohr, H. Hübel, A. Görgen, G. Schönwasser, A. Bracco, S. Leoni, A. Maj, C.M. Petrache, P. Bednarczyk, D. Curien, Phys. Rev. Lett. **86**, 5866 (2001).
11. D.R. Jensen, G.B. Hagemann, I. Hamamoto, S.W. Ødegård, M. Bergström, B. Herskind, G. Sletten, S. Törmänen, J.N. Wilson, P.O. Tjøm, K. Spohr, H. Hübel, A. Görgen, G. Schönwasser, A. Bracco, S. Leoni, A. Maj, C.M. Petrache, P. Bednarczyk, D. Curien, Nucl. Phys. A **703**, 3 (2002).
12. A. Bohr, B.R. Mottelson, *Nuclear Structure*, Vol. **II** (Benjamin, Reading, MA, 1975).
13. T. Døssing, B. Herskind, S. Leoni, A. Bracco, R.A. Broglia, M. Matsuo, E. Vigezzi, Phys. Rep. **268**, 1 (1996).
14. M. Matsuo, T. Døssing, E. Vigezzi, R.A. Broglia, K. Yoshida, Nucl. Phys. A **617**, 1 (1997).
15. B. Lauritzen, T. Døssing, R.A. Broglia, Nucl. Phys. A **457**, 61 (1986).
16. S. Leoni, A. Bracco, T. Døssing, B. Herskind, J.C. Lisle, M. Matsuo, E. Vigezzi, J. Wrzesinski, Eur. Phys. J. A **4**, 229 (1999).
17. J. Simpson, Z. Phys. A **358**, 139 (1997).
18. O. Andersen, J.D. Garrett, G.B. Hagemann, B. Herskind, D.L. Hillis, L.L. Riedinger, Phys. Rev. Lett. **43**, 687 (1979).

19. D.C. Radford, Nucl. Instrum. Methods A **361**, 297 (1995).
20. S. Leoni, Ph.D. Thesis, University of Milano (1992).
21. K. Yoshida, M. Matsuo, Nucl. Phys. A **636**, 169 (1998).
22. S. Leoni, T. Døssing, A. Bracco, S. Frattini, G. Montingelli, E. Vigezzi, M. Bergström, G.B. Hagemann, B. Herskind, M. Matsuo, Nucl. Phys. A **671**, 71 (2000).